X-ray microtomography analysis of soil pore structure dynamics under wetting and drying cycles

Luiz F. Pires[a], André C. Auler[b], Waldir L. Roque[c] and Sacha J. Mooney[d]

[a] *Laboratory of Physics Applied to Soils and Environmental Sciences, Department of Physics, State University of Ponta Grossa (UEPG), 84.030-900, Ponta Grossa, PR, Brazil*

[b] *Department of Soils and Agricultural Engineering, Federal University of Paraná, 80.035-050, Curitiba, PR, Brazil*

[c] *Petroleum Engineering Modelling Laboratory, Department of Scientific Computation, Federal University of Paraíba, 58.051-900, João Pessoa, PB, Brazil*

[d] *Division of Agricultural and Environmental Sciences, School of Biosciences, University of Nottingham, Sutton Bonington Campus, Leicestershire LE12 5RD, UK*

Corresponding author:

Prof. Dr. Luiz F. Pires, Phone: (55) 42 3220 3044. Fax: (55) 42-3220-3042

E-mail: luizfpires@gmail.com; lfpires@uepg.br (Luiz F. Pires).

Proofs should be sent to:

Prof. Dr. Luiz Fernando Pires, Departamento de Física, Universidade Estadual de Ponta Grossa, Campus de Uvaranas, Bloco L, Sala 15B; Av. Carlos Cavalcanti, 4748, CEP 84.030-900, Ponta Grossa, PR, Brazil.

X-ray microtomography analysis of soil pore structure dynamics under wetting and drying cycles

L.F. Pires[a,1], A.C. Auler[b], W.L. Roque[c] and S.J. Mooney[d]

[a] *Laboratory of Physics Applied to Soils and Environmental Sciences, Department of Physics, State University of Ponta Grossa (UEPG), 84.030-900, Ponta Grossa, PR, Brazil*

[b] *Department of Soils and Agricultural Engineering, Federal University of Paraná, 80.035-050, Curitiba, PR, Brazil*

[c] *Petroleum Engineering Modelling Laboratory, Department of Scientific Computation, Federal University of Paraíba, 58.051-900, João Pessoa, PB, Brazil*

[d] *Division of Agricultural and Environmental Sciences, School of Biosciences, University of Nottingham, Sutton Bonington Campus, Leicestershire LE12 5RD, UK*

ABSTRACT

The soil water retention curve is one of the most important properties used to predict the amount of water available to plants, pore size distribution and hydraulic conductivity, as well as knowledge for drainage and irrigation modeling. Depending on the method of measurement adopted, the water retention curve can involve the application of several wetting and drying (W-D) cycles to a soil sample. The method assumes soil pore structure is constant throughout however

[1] Corresponding authors.
Tel.: +55 42 3220-3044
E-mail addresses: luizfpires@gmail.com; lfpires@uepg.br (L.F. Pires)

most of the time soil structure is dynamic and subjected to change when submitted to continuous W-D. Consequently, the pore size distribution, as well as other soil morphological properties can be affected. With this in mind, high resolution X-ray Computed micro-Tomography was utilized to evaluate changes in the soil pore architecture following W-D cycles during the procedure of the water retention curve evaluation. Two different soil sample volumes were analyzed: ROI_W (whole sample) and ROI_{HC} (the region close to the bottom of the sample). The second region was selected due to its proximity to the hydraulic contact of the soil with the water retention curve measurement apparatus. Samples were submitted to the following W-D treatments: 0, 6 and 12 W-D. Results indicated the soil changed its porous architecture after W-D cycles. The image-derived porosity did not show differences after W-D cycles for ROI_W; while for ROI_{HC} it increased porosity. The porosity was also lower in ROI_{HC} in comparison to $ROI_{W.}$ Pore connectivity improved after W-D cycles for ROI_{HC}, but not for ROI_W. W-D cycles induced more aligned pores for both ROIs as observed by the tortuosity results. Pore shape showed changes mainly for ROI_W for the equant and triaxial shaped pores; while pore size was significantly influenced by the W-D cycles. Soil water retention curve measurements showed that W-D cycles can affect water retention evaluation and that the changes in the soil morphological properties can play an important role in it.

Keywords: Soil structure; Pore shape; Pore size distribution; Soil micromorphology; 3D image analysis.

1.INTRODUCTION

The soil water retention curve is a very important soil physical-hydraulic property, expressed by the relationship between the pressure head of the soil and its water content (Klute, 1986). The soil water retention curve can be used to evaluate different parameters such as the amount of water available to the plants, field capacity, permanent wilting point, pore size distribution, etc. (Hillel, 2004; Radcliffe and Simunek, 2010). The methods used to determine this property typically require equipment such as suction tables, pressure chambers, gamma-ray sources and tensiometers (Smagin, 2012; Braudeau et al., 2014).

The relation between the pressure head and soil water content can be obtained in two ways, desorption (drying) and sorption (wetting). Continuous curves are obtained in both methods, but in general, they are not identical due to hysteresis (Hillel, 2004). The soil water retention curve determination involves the measurement of a series of equilibria of the water in the soil sample at known pressure heads. Depending on the experimental procedure chosen samples can be submitted to several wetting and drying (W-D) cycles (Moraes et al., 1993; Kong et al., 2018; Reis et al., 2019).

Moraes et al. (1993) presented an analysis of methodological problems during evaluation of the water retention curve examining 250 curves obtained through suction tables and pressure chambers. They verified 43% of the samples did not show consistent results and pointed out that effective hydraulic contact is crucial for the evaluation of representative SWRCs. Additionally, soil structure changes caused by the application of W-D cycles can affect the water retention curve quality (Bacchi et al, 1998; Pires et al., 2008a; Liu et al., 2012; Sayem and Kong, 2016; Zhang et al., 2017; Kong et al., 2018). The rearrangement of particles inside the soil matrix affecting soil resistance, particle cohesion, internal

friction, clay dispersion, aggregate size and stability can be induced by the application of W-D (Rajaram and Erbach, 1999).

Thus, possible changes in soil pore structure in different regions of the soil sample could help to explain differences in water retention curve when samples are submitted to several W-D (Hussein and Adey, 1998; Pires et al., 2005; Pires et al., 2008a; Zhang et al., 2017). One part of the soil sample that is of particular interest is the region close to the hydraulic contact to the porous plate or sandbox. It is known that when the water flows from the soil to the porous plate changes in the hydrostatic pressure distribution occur. These modifications can affect the quality of data from the sample in regions close to the hydraulic contact associated with the interface between the soil sample bottom and the porous plate or sand (Alagna et al., 2016).

Imaging techniques such as X-ray Computed micro-Tomography offer great potential as a tool to visualize and subsequently better understand how changes in the soil pore structure might arise from W-D and thus their impact on the water retention curve. X-ray microtomography is a non-invasive and non-destructive technique that allows the study of morphological properties of the structure of the soil (Peth et al., 2008; Smet et al., 2017; Cássaro et al., 2017; Galdos et al., 2019; Pires et al., 2019). X-ray microtomography has been utilized for the analysis of soils since the the 1980s (Petrovic et al., 1982). The ability to undertake three-dimensional (3D) analysis allows the evaluation of several soil structural properties such as porosity, number of pores, pore size, pore shape, fractal dimension, anisotropy, connectivity and tortuosity (Luo et al., 2010; Garbout et al., 2013; Dal Ferro et al., 2014; Borges et al., 2018; Ferreira et al., 2019; Diel et al., 2019).

Microtomography can provide important insights into how W-D affects soil pore structure at the microscale. Ma et al. (2015) analyzed changes in soil structure caused by W-D through synchrotron-based X-ray microtomography. They observed significant alterations in the soil porosity, pores >100 μm and in the fraction of elongated pores. Helliwell et al. (2017) observed significant changes in the soil structure in repacked cores after a single wetting and drying event, though further W-D had little impact. Further studies that evaluate modifications in soil pore structure in 3D at micrometric scale are scarce. Conversely, many studies have analyzed the effect of W-D in soil pore structure in two-dimensions (2D) (Sartori et al., 1985; Pagliai et al., 1987; Pires et al., 2008b; Rasa et al., 2012). However, 2-D images of pore structure only provide information about the area, perimeter, diameter, arrangement and size distribution of pores, which fails to account for the true heterogeneity of the soil structure (Bouma et al., 1977).

The aim of this study was to verify how alternations of W-D modify the soil pore structure morphological properties. Two sample volumes were analyzed: the first comprised almost the whole sample and the second, a small region close to the bottom of the sample. We hypothesized that there would be changes in the morphological properties of the soil as a consequence of W-D that affects the region close to the bottom of the sample differently in relation to the whole sample.

2.MATERIALS AND METHODS

2.1 Experimental site and soil sampling

Soil samples were obtained from an experimental field under zero tillage at the soil research unit of the Agricultural Research Institute of Parana (IAPAR) in the city of Ponta Grossa, PR, Brazil (25°06'S, 50°10'W, 875 m above sea level). The soil was an Oxisol (Rhodic Hapludox) according to USDA soil taxonomy (Soil Survey Staff, 2013). The soil was classified as a clay texture with 17% sand, 30% silt and 53% clay. The particle density and the amount of C content evaluated were 2.41 g cm^{-3} and 60.7 g kg^{-1}, respectively.

Soil sampling was carried out at the beginning of 2017 from the surface layer (0-10 cm) after corn harvest in the middle of the crop interrows to avoid possible effects of tractor wheel traffic (cleaning, plant seed and soil preparation operations) on the soil structure. Undisturbed samples were collected in steel cylinders (c. 5 cm high and c. 5 cm diameter), with the help of an Uhland sampler, for the microtomography (9 samples) and soil water retention curve (18 samples) analysis. Sampling was undertaken very carefully, in order to prevent soil compaction during extraction and handling. The choice of samples collected in cylinders for this study was due to their use for water retention curve measurements. Since the soil water content is very important at the sampling time, to minimize damage in the soil structure, samples were collected when soils were near their field capacity, about three days after a high intensity rainfall event.

2.2 Wetting and drying cycles (W-D) for microtomography analysis

Soil samples were saturated by the capillary rise method. The wetting (W) procedure consisted in soaking the samples in a tray with the water level just below the top of the steel cylinders. This procedure was kept over a period of 2

142 days to allow saturation of the sample and to avoid the presence of the entrapped
143 air bubbles, which can cause slaking of soil aggregates (Klute, 1986). Samples
144 were partially dried by submitting them to a pressure head of -60 cm of H_2O on a
145 suction table (Eijkelkamp 08.01 Sandbox for pF determination). After reaching
146 the thermodynamic equilibrium, the samples were again saturated and submitted
147 to a new suction application (new drying) to simulate a series of W-D. This wetting
148 and drying procedure was exactly the same as that employed to evaluate soil
149 water retention curves (Klute, 1986). Three treatments were investigated: 0 W-D,
150 in which samples were not submitted to any wetting and drying cycle, 6 and 12
151 W-D cycles.

152 *2.3 Soil water retention curve measurement*

153 The wetting procedure to saturate the samples was exactly the same as
154 that described in the previous section. Following the saturation, the samples were
155 placed in contact with the porous media (sand) on the suction table. The samples
156 were equilibrated in the pressure heads varying from -10 to -100 cm of H_2O with
157 intervals of 10 cm (Romano et al., 2002). After the thermodynamic equilibrium
158 was reached (nearly 4-5 days for each sample) the moist soil mass was evaluated
159 using a precision balance (0.01 g). The dry soil mass was obtained at the end of
160 the water retention curve by oven drying for 48 h at 105 °C.

161 The experimental pairs of data obtained (soil water contents and pressure
162 heads) were fitted using the mathematical model proposed by van Genuchten-
163 Mualem equation (van Genuchten, 1980). The Excel solver based on the total
164 sum of squares was used for fitting the experimental data. The soil water retention
165 curve adjustments were obtained using the average values of soil water contents
166 (n=6). In order to check the quality of the water retention curve fitting, the root-

mean-square error and the coefficient of determination were calculated. Relative differences (RD) were also obtained between the water retention curves in order to evaluate the effect of the different W-D on the soil pore structure.

2.4 Computed Tomography

The soil samples were carefully extracted from the steel cylinders before the microtomographic analysis to avoid the influence of the steel cylinder in the flux of X-ray photons. Prior to the scanning, the samples were coated with paraffin wax to minimize potential movement during transport from Brazil to the UK. More details about paraffin wax coating were described by Pires et al. (2019). This procedure was carried out after the application of the cycles for each treatment. Before coating, the samples were partially dried at 40 ^{o}C until their mass became constant. Each soil sample was scanned using a G.E. V-Tomex-M X-ray Computed Tomography scanner (GE Measurement & Control Solutions, Wunstorf, Germany) at the Hounsfield Facility (University of Nottingham, Sutton Bonington Campus, UK).

The voltage, current and integration time adopted for the image acquisition process were 180 kV, 160 µA and 250 ms. A 0.1 mm Cu-filter was used to minimize beam-hardening effects. A total of 2520 projections were obtained per sample with a voxel resolution of 35 µm. The radiographs of each scan were reconstructed in 32 bit format in order to prevent compression of the greyscale histogram. The gray scale of all 16-bit images was calibrated to values based on the brightest (Mineral) and darkest (Air) objects in all of samples and then a grey level value was set based on the calculation of 2,661 for air and 47,092 brightest mineral (in 16-bit depth). However, despite taking great care it is not possible to eliminate all potential scanning artefacts.

After reconstruction, the images were imported into Volumetric Graphics StudioMAX® 2.0 and cropped to a cubic shape (ROI_W) with 29.8 × 29.8 × 29.8 mm (850 × 850 × 850 voxels). ROI_W was selected a few centimeters from the edge of the samples to minimize any influence of the paraffin wax in the soil structure (Pires et al., 2019). Another region of interest (ROI_{HC}) smaller than the first one was also evaluated. This smaller region sized 29.8 × 29.8 × 7.0 mm (850 × 850 × 200 voxels) was selected inside the largest one, 2.45 mm away from the bottom of the sample.

Although the great interest in selecting the ROI_{HC} was to analyze the effect of W-D cycles in the region of hydraulic contact; unfortunately, it was impossible to select the exact region of the sample in which hydraulic contact with the sandbox occurs. The main reasons for that were the sample coating procedures, the irregularities in sample shape in this region and imaging artifacts at the edge of samples.

The original grey-level X-ray microtomographic images were processed using ImageJ 1.42 software (Rasband, 2007). An *unsharp mask* procedure with 1 voxel standard deviation and weighing 0.8 was applied to enhance the edge contrast. The segmentation process was based on the nonparametric and unsupervised Otsu method for thresholding (Otsu, 1979). The *remove outlier* tool with a 0.75 radius was applied to the images after segmentation. This process resulted in a binary image, in which pores and solids were represented by white and black pixels.

For the assessment of 3D soil structure, pores were classified according to their shape and size distribution. For the shape classification, geometrical parameters known as major, intermediate and minor axes of the ellipsoids that

represent each pore were determined using 3D measuring techniques. These parameters were measured using the *Particle Analyser* tool in the ImageJ. Isolated pores <9 voxels were removed from the porous fraction of the images for the analyses of pore size and pore shape distribution to avoid potential dubious features from unresolved voxels (Jefferies et al., 2014).

The soil pores which allowed the measurement of the three main axes were classified according to the terminology suggested by Zingg (1935). The relation between the ratio of the intermediate by the major (Int./Maj.) axis and the ratio of the minor by the intermediate (Min./Int.) axis allows pore classification based on shape. Therefore, the pore shapes were classified as: Equant (EQ), Prolate (PR), Oblate (OB), and Triaxial (TR) (Pires et al., 2017).

The image-derived porosity and number of disconnected pores were calculated considering all resolvable pores. In this study, the term porosity refers to soil macropores only. The 3D pore size distribution was determined based on the volume of pores classified in different logarithmic volume intervals: 0.001-0.01; 0.01-0.1; 0.1-1; 1-10; and >10 mm^3.

The X-ray microtomographic images were also analyzed in terms of tortuosity of the pore network using the Osteoimage software (Roque et al., 2009). The tortuosity, which is geometrically defined by the ratio between the geodesic distance between two connected points and the Euclidean distance between these two points, was calculated through the geodesic reconstruction algorithm (Roque et al., 2012). The characteristic of Euler-Poincaré was utilized to estimate the degree of connectivity, which represents one of the Minkowski functions and a topological measure used for describing the connectivity of spatial structures (Vogel and Roth, 2001; Vogel et al., 2010; Katuwal et al., 2015). This

parameter is related to the number of isolated parts minus the connectivity of an object (Thurston, 1997). Based on Euler-Poincaré values, the Euler-Poincaré per sample volume was evaluated. The Euler-Poincaré number is an indicator of how well connected a pore network is: the smaller (more negative) it is, the higher the pore connectivity is (Roque et al., 2009). The degree of anisotropy, which gives the preferred orientation of pores, was determined in 3D by using the Bone J plugin (Doube et al., 2010). The pore volume interconnectedness was characterized by network properties. The *3D skeletonize* plugin (Image J) was applied to reduce iteratively the diameter of pores until only a skeleton was obtained. Parameters such as number of junctions and number of branches were measured using the Image J plugin *analyse skeleton*.

2.5 Statistical analysis

The data obtained via image analysis and water retention curve were submitted to Shapiro-Wilk and Bartlett tests to verify normality and homoscedasticity, respectively. When pre-suppositions had been verified ($p > 0.05$), since this is a nonparametric study, orthogonal contrasts between ROIs for each W-D cycle and among W-D cycles for each ROI were employed. To obtain the significance ($p \leq 0.05$) of the orthogonal contrast the Student t-test was applied. Simple linear correlation was performed by analyzing the Pearson's correlation coefficients. All data were analyzed using the software R, version 3.6.1 (R Core Team, 2018).

3.RESULTS AND DISCUSSION

3.1 Morphological properties of porous system

The porosity analyzed for the whole sample (ROI_W) showed differences between 6 and 12 W-D cycles, as well as in relation to 0 W-D. However, for the region closer to the hydraulic contact (ROI_{HC}), the action of 6 and 12 W-D cycles increased porosity in relation to control but did not differ from each other. Soil porosity was also lower in ROI_{HC} in comparison to ROI_W for all W-D cycles, which means there were differences in the pore distributions inside the samples (Fig. 2a). The lower image-derived porosity for the lower portion of the samples may have been influenced by the procedures utilized for collecting samples in volumetric rings; as regions close to the walls of the cylinders can be subjected to stresses which damage the soil structure. Pires et al. (2004) has previously showed, through computed tomography imagery, the effects of different cylinder diameters in the soil structure due to sampling. As the lower region of the sample presented a decrease in its porosity, few wetting and drying cycles can provoke important changes in its structure. This was observed in our work for ROI_{HC}, when 6 W-D cycles caused the most important changes in the soil structure for this region.

The number of pores increased after the application of 12 W-D cycles in relation to 0 and 6 W-D only for ROI_W, while for ROI_{HC} no effects of W-D cycles were observed (Fig. 2b). We also noticed that the number of pores did not differ between ROI_W and ROI_{HC} for all W-D cycles analyzed. However, soil pore structure changes as shown by the porosity increase were not influenced by the increase in the number of pores after W-D cycles mainly for ROI_{HC} (Table 1).

The application of W-D cycles can provoke swelling and shrinkage processes in the soil volume, which cause tension forces between aggregates. The action of these forces can reduce soil porosity when the force is directed

290 from the border to the center of the aggregates, which takes place during sample
291 drying. Schlüter et al. (2016) observed that the soil deformation, as consequence
292 of shrinkage, occurs in any drying process for swelling clay minerals. According
293 to these authors the capillary forces that pull unconsolidated grains close together
294 can also cause changes in soil structure in drying processes. When the soil is
295 submitted to wetting, the force follows the opposite direction from the center to
296 the borders of the aggregates, which increases soil porosity (Peng et al., 2007;
297 Bodner et al., 2013). As the samples may have been submitted to some damage
298 during sampling, this may also help to explain the differences observed between
299 regions of interest (ROI_W and ROI_{HC}). The possible compaction induced by
300 sampling in specific regions of the sample has higher capacity to recover the
301 structure towards higher porosities than in the case of non-compacted samples.

302 Pore architecture modifications due to repeated W-D cycles have been
303 described by several authors with potential reasons for this identified as a
304 consequence of internal forces, including air entrapment and expansion between
305 aggregates, natural reconsolidation of aggregates, aggregate fragmentation and
306 generation of soil cracks (Tessier et al., 1990; Hussein and Adey, 1995; Li et al.,
307 2004; Tang and Shi, 2011; Diel et al., 2019). As a consequence, those authors
308 reported the main modifications in the soil pore structure as a function of W-D
309 cycles usually occur in the size and shape of aggregates and pores, porosity,
310 pore orientation and pore connectivity (Pardini et al., 1996; Hussein and Adey,
311 1998; Peng et al., 2007; Tracy et al., 2015; Zhang et al., 2018).

312 During W-D cycles, the pressure caused by the water movement until the
313 hydraulic equilibrium is reached by the samples can cause the removal of clay
314 particles from the surface of soil aggregates, which might reduce their stability

315 (Czyż and Dexter, 2015; Ma et al., 2015). The dispersed particles could: (i)
316 migrate to ROI_{HC} sealing the pores located at the bottom of the sample in contact
317 to the sandbox decreasing soil porosity (Zhang et al., 2014 ; Périard et al., 2016)
318 or (ii) be removed from the samples to the sandbox (Reynolds and Topp, 2006;
319 Pires et al., 2011). The latter, which simulates the eluviation/illuviation processes
320 in the soil profile, would be dependent on the pressure head applied to the sample
321 as well as the characteristics of the dispersed clay (Czyż and Dexter, 2015).

322 However, it is important to mention that different soil types are likely to
323 present different results than the observed in our study. Clay minerals present in
324 the soil can differ considerably in several properties such as specific surface,
325 shape, volume, etc., which will influence the clay particle dynamics under wetting
326 and drying (Jury and Horton, 2004). For example, we would expect less severe
327 changes in the soil structure due to the W-D cycles for sandy in the comparison
328 to clayey soils, as investigated in our work. This is related to the main minerals
329 that compose the sandy soils and their capacity to pack and hold together the
330 particles in aggregate form, which will influence the production of intra and inter-
331 aggregate pores (Hillel, 2004).

332 Soil pore structure was not affected by the concentration of dispersed clay
333 in ROI_{HC}, since decreases in soil porosity were not observed after the application
334 of W-D cycles (Fig. 2a). The results show the forces acting on drying probably
335 overcome those acting on wetting (Bodner et al., 2013). The decrease in
336 tortuosity (Fig. 3 and Table 1), with the application of W-D cycles can be
337 considered as evidence of this hypothesis, because an interconnection of the
338 pores can be related to more continuous flow channels (Peth et al., 2008).

339 The soil pore architecture modifications due to W-D cycles did not cause
340 heterogeneities in the pore distributions in ROI_{HC} as verified by the anisotropy
341 results. In relation to ROI_{W}, both 6 and 12 W-D cycles reduced the degree of
342 anisotropy in comparison to the samples not submitted to W-D cycles.
343 Considering the W-D cycles, the different regions studied did not differ from each
344 other in terms of anisotropy (Fig. 2c). Similar results were found by Piccoli et al.
345 (2019), who found that the anisotropy of the soil is not affected by the sample
346 volume; although tillage processes can affect significantly this property (Piccoli et
347 al., 2017).

348 Pore connectivity increased after 6 and 12 W-D cycles for ROI_{HC} and
349 ROI_{W}. ROI_{HC} had a higher pore connectivity than ROI_{W}. The soil pore structure in
350 ROI_{HC} was greatly influenced by W-D cycles in terms of pore connectivity (Fig.
351 2d). The increase in pore connectivity for ROI_{HC} was also followed by an increase
352 in the number of junctions and branches of pores induced by the cycles in relation
353 to 0 W-D. This result could also help to explain the increase in soil porosity
354 following W-D cycles. The number of junctions and branches was also affected
355 by the number of W-D cycles for ROI_{W} (Figs. 2e, f) with lower values compared
356 to ROI_{HC}. This is an indication of a more complex soil structure in the region close
357 to the bottom of the sample in relation to the whole sample as a result of
358 reorganization of some kind.

359 The increase in the porosity influenced positively the number of junctions
360 and branches and negatively the pore connectivity for ROI_{W} and ROI_{HC} (Table 1).
361 However, pore connectivity was not affected by the increase in the number of
362 pores for ROI_{W} and ROI_{HC}, although for ROI_{W} the number of junctions were

363 positively correlated to the number of pores. This result could be explained by the
364 larger volume of sample analyzed for ROI_W.

365 The increase in pore connectivity was accompanied by a decrease in the
366 number of junctions and branches mainly for ROI_{HC}, which was more susceptible
367 to changes in relation to the whole sample (Table 1). For ROI_W the increase in
368 the porosity with the W-D cycles was followed by a decrease in anisotropy and
369 an increase in pore connectivity. For ROI_{HC} no significant correlations for
370 anisotropy were observed.

371 The average tortuosity and the tortuosity in the different directions
372 decreased for both ROIs with W-D cycles (Fig. 3). The region close to the bottom
373 of the samples was characterized by a higher tortuosity than the whole sample
374 (ROI_W). This result was independent on the W-D cycles. We expected an
375 increase in tortuosity with the cycles due to the increase observed in the number
376 of junctions and branches. However, this was not observed in our study.

377 The decrease in the average tortuosity was followed by an increase in pore
378 connectivity and in the number of junctions and branches for ROI_W and ROI_{HC}
379 (Table 3). These results indicate that more aligned pores were characterized by
380 a greater number of connected pores, mainly for ROI_{HC}. This is interesting
381 because these two morphological properties are known to influence water
382 movement (Sayem and Kong, 2016). Since the water movement from the bottom
383 of the sample to the sandbox is greatly dependent on the soil pore structure,
384 changes in pore connectivity and tortuosity can have important influence in the
385 soil water retention curve evaluation due to W-D cycles (Figs. 2d and 3) (Pires et
386 al., 2008a; Rafraf et al., 2016). Dörner and Horn (2006) pointed out that even
387 when small changes in soil porosity are observed, significant modifications in

pore continuity and geometry can present great influence on soil hydraulic properties.

3.2 Pore shape and size distributions

The distribution of pore sizes was affected by the W-D cycles for ROI_W and ROI_{HC} (Fig. 4). Volume of pores presented a significant decrease between 0.0001-0.01, 0.01-0.1, 0.1-1 and 1-10 mm^3 pore size classes after 6 and 12 W-D cycles in comparison to the control treatment (Figs. 4a to 4d). For the different ROIs analyzed the same behavior was noticed between 0, 6 and 12 W-D cycles, except for 12 W-D cycles for pores with sizes between 0.1 and 1 mm^3 (Fig. 4c). The influence of these pore classes in soil porosity was greater for ROI_{HC} in comparison to ROI_W (Figs. 4a, b).

For the largest pores (>10 mm^3), the ROI_W volume of pores was significantly larger than that of ROI_{HC} for 0, 6 and 12 W-D cycles (Fig. 4e). Volume of pores also increased with the application of W-D cycles for the largest pore sizes for ROI_{HC} and ROI_W. This result explains the increase in soil porosity (Table 1), which is related to an increase in the number of pores joined together.

Several authors have reported increases in the volume of large pores in clayey soils following W-D cycles, as a consequence of textural effects and interlayer swelling at microscopic and macroscopic scales (Sartori et al., 1985; Pires et al., 2008b; Zemenu et al., 2009; Peng et al., 2007; Ma et al., 2015). Bodner et al. (2013) demonstrated the intensity of W-D increases the macroporosity for soils with more stable structures, such as those found under zero-tillage management. The increase in the volume of large pores will certainly

411 impact water retention for high pressure heads due to lower capillary forces
412 caused by larger pores (Périard et al., 2016).

413 Significant correlations were found between the distribution of pore sizes
414 and the micromorphological properties studied as a function of W-D cycles, which
415 showed different behavior between ROI_{HC} and ROI_{W} (Table 1). The increase in
416 soil porosity and volume of pores (>10 mm^3) (positive correlation) produced a
417 more heterogeneous soil structure, which was confirmed by the results of the
418 number of junctions and branches. A high density of branches and junctions is
419 related to an extensive, well-connected and complex pore network (Peth et al.,
420 2008; Munkholm et al., 2012). However, the tortuosity was the converse (Table
421 1), which can be explained by the great influence of larger macropores to soil
422 porosity. Samples presenting a high volume of pores (>10 mm^3) are normally
423 characterized by a large number of junctions and branches when all the pores
424 from 3D images are analyzed (Garbout et al., 2013). According to our results
425 (Table 1), we reinforce the importance of these changes mainly when occurring
426 in the region close to the bottom of the sample (ROI_{HC}).

427 The distribution of pores in terms of shape presented differences between
428 ROIs with the W-D cycles for the equant and triaxial shaped pores (Fig. 5). The
429 cycles caused an increase in the equant shaped volume of pores for $ROI_{W,}$ while
430 the opposite was observed for ROI_{HC} (Fig. 5a). For the triaxial shaped pores, a
431 decrease in these pore types was recorded for ROI_{W} (Fig. 5d). Few significant
432 correlations were measured between the distribution of pores in terms of shape
433 and the micromorphological properties investigated, mainly for ROI_{HC} (Table 1).
434 For ROI_{W}, pore shape was related with pore connectivity and tortuosity in the x
435 and z directions. The increase in the equant and prolate shaped pores and the

436 decrease in triaxial shaped pores influence the volume of pores that are related
437 to an increase in pore connectivity. This was also observed for the average
438 tortuosity and the tortuosity in the different directions. Only the triaxial shaped
439 volume of pores variation was not related to tortuosity (Table 1). Differences in
440 the pore shape distribution are important because there is a close correlation
441 between pore shape and water retention and movement in the soil (Pagliai and
442 Vignozzi, 2002; Yoon et al., 2007).

443 However, it is important to mention that > 60% of the pores were
444 not classified as they had a complex shape that is probably related to the
445 junctions of the poresfollowing the application of the W-D cycles.

446 *3.3 Soil water retention*

447 The water retention curves showed the W-D cycles treatment influence in
448 the soil structure. In our study computed tomography was used to reveal the
449 structural arrangements of the soil sample following W-D treatment and not
450 compare the pore size distribution with the water retention curve. The pressure
451 head range was selected according to the resolution of the microtomographic
452 images. However, the water retention data allowed us only to analyze pores
453 smaller than the resolution obtained by computed tomography imagery, *i.e.*,
454 textural pores.

455 The soil water retention curve was most influenced by the application of
456 12 W-D cycles as observed by the van Genuchten-Mualem model parameters
457 (Table 2). Higher water retention was found for the range of pressure heads
458 analyzed with 12 W-D cycles (Fig. 6a). This implies that the application of 12 W-
459 D caused an increase in pores from to textural to structural pore size ranges (from

460 30 to >100 µm equivalent cylindrical diameter), *i.e.*, medium to coarse pores. This
461 result is partially supported by the computed tomography data (Fig. 4). The
462 application of W-D cycles can promote changes in fine matrix pores especially
463 when clayey soils are dried due to the susceptibility of the soil to swelling and
464 shrinkage. W-D cycles can also cause changes in the largest pores as in our
465 study which helps to explain the results for the water retention for 12 W-D cycles
466 (Fig. 4e).

467 Differences of around 10% were recorded between -5 to -100 cm when
468 the samples were submitted to 12 W-D in relation to 0 W-D cycles (Fig. 6b).
469 However, the application of 6 W-D cycles did not appear to generate significant
470 changes in the soil structure in relation to the control samples (0 W-D). This result
471 was not expected considering the results of porosity and pore size distribution
472 obtained via computed tomography imagery. However, it is important to note that
473 the samples utilized for the water retention analysis were not the same as those
474 used in computed tomography analysis; thus spatial variability could influence the
475 results observed. Zhou et al. (2017) pointed out that it is hard to compare results
476 from computed tomography and water retention due to the differences between
477 methods and the soil pore range over different orders of scale.

478 The largest difference between 0 and 6 W-D cycles was around 2% for -
479 20 to -100 cm (Fig. 6b). This means that only after the application of more than 6
480 W-D cycles, the soil under zero-tillage presented important modifications to its
481 structure. This was confirmed by the comparison between 6 and 12 W-D cycles.
482 The largest difference observed was around 9% for between -5 and -60 cm (Fig.
483 6b). Denef et al. (2001a,b) reported the amount of large macroaggregates was
484 reduced after the first W-D and after the second cycle they became stable and

485 resistant to disintegration. Zhang et al. (2018) pointed out that depending on the
486 experimental setup and the soil texture, a large number of W-D can be necessary
487 to cause important changes in soil structure. Similar results were found by Pires
488 et al. (2005) working with clay and sandy Brazilian soils.

489 To understand the dependence on changes in morphological properties of
490 the soil pore structure and water retention, a correlation analyses were carried
491 out between these properties and van Genuchten-Mualem fit parameters for
492 ROI_W (Table 3) but only a few parameters presented any correlation. Possible
493 explanations are: (i) the computed tomography analysis was not performed on
494 the same samples of soil water retention curve evaluation as previously
495 mentioned, (ii) the volume of analysis considered was not the same between the
496 two techniques and (iii) the resolution limitation of computed tomography imaging
497 used in this study only allows the evaluation of mainly pores classified as
498 structural pores (Zhou et al., 2017).

499 The parameter α was inversely related to the soil porosity, number of
500 pores, number of junctions and showed a positive correlation with pore
501 connectivity, volume of pores between 0.1-1 and 1-10 mm^3 and tortuosity in x-
502 direction (Table 3). This parameter allow us to evaluate what happens with the
503 large structural pores close to the water saturated region of the measured water
504 retention curves (Bruand and Cousin, 1995). Smaller values of α are directly
505 related to decreases in structural pores (Stange and Horn, 2005). We observed
506 that the contribution of structural pores to the soil porosity was affected by W-D
507 cycles, especially after 12 W-D cycles (Fig. 4). The parameter n was inversely
508 related to the soil porosity, number of pores, number of junctions and branches
509 and volume of pores >10 mm^3; and positively related to the average tortuosity,

510 the tortuosity in the x and z-directions, the volume of pores between 0.01-0.1,
511 0.1-1 and 1-10 mm^3 (Table 3). This parameter indicates the difference in the
512 amount of water retained between 0 and -100 cm which was small for 6 and 12
513 W-D, in the comparison to 0 W-D cycles. This result shows clear evidence of the
514 effect of changes in the distribution of pore sizes with the application of W-D
515 cycles (Fig. 4).

516 However, the fact that only few morphological properties correlated with
517 the water retention van Genuchten-Mualem fitting parameters shows the difficult
518 in trying to comparing soil physical properties from methods that consider
519 measurements across different spatial scales. The limited number of soil samples
520 investigated in this study may also contribute to the lack of correlations among
521 the majority of the parameters analyzed.

522 4. CONCLUSIONS

523 Soil samples can exhibit distinct changes in their pore architecture
524 structure, as well as water retention, as function of repeated W-D cycles. The soil
525 close to the hydraulic contact with the sandbox as part of measurement of the
526 water retention curve presented similar behavior to the rest of soil sample which
527 was surprising as the pore connectivity and tortuosity measured by computed
528 tomography imagery was greatly affected by W-D cycles for this region. The
529 water movement in the soil towards the sandbox is greatly influenced by these
530 two parameters, which would be expected to affect the representativeness of the
531 water retention curve. The application of both 6 and 12 W-D cycles increased the
532 image-derived soil porosity, volume of larger pores and pore connectivity in
533 ROI_{HC}. The tortuosity of the pore network was reduced with the application of W-
534 D cycles, especially in ROI_{HC}. When considering the water retention curve the

differences were mainly observed in samples which were submitted to 12 W-D cycles, which had an increase the amount of water retained for the structural and textural pores. Though, we note in this study, only a clay textured soil was considered in which the structural rearrangement following W-D is enhanced compared to a coarser textured soil such as predominantly sandy soils.

ACKNOWLEDGEMENTS

LFP would like to acknowledge the financial support provided by the Brazilian National Council for Scientific and Technological Development (CNPq) and the Coordination for the Improvement of Higher Education Personnel (Capes) through the Grants 303726/2015-6 (Productivity in Research) and 88881.119578/2016-01 (Visiting Scholar). We acknowledge the laboratory and computational work from Dr. Brian Atkinson from the Hounsfield Facility at the University of Nottingham and MS. Jocenei A.T. Oliveira. SM is funded by NUCLEUS: a virtual joint centre to deliver enhanced NUE via an integrated soil-plant systems approach for the United Kingdom and Brazil. This work was supported by FAPESP—São Paulo Research Foundation [Grant 2015/50305-8]; FAPEG—Goiás Research Foundation [Grant 2015-10267001479]; FAPEMA—Maranhão Research Foundation [Grant RCUK-02771/16]; and the Biotechnology and Biological Sciences Research Council [grant number BB/N013201/1]

REFERENCES

Ahuja, L.R., Fiedler, F., Dunn, G.H., Benjamin, J.G., Garrison, A., 1998. Changes in soil water retention curves due to tillage and natural reconsolidation. Soil Sci. Soc. Am. J. 62, 1228–1233.

Alagna, V., Bagarello, V., Di Prima, S., Iovino, M., 2016. Determining hydraulic properties of a loam soil by alternative infiltrometer techniques. Hydrol. Process. 30, 263-275.

Andrade, A.P., Mafra, A.L., Baldo, G.R., Piccolla C.D., Bertol, I., Albuquerque, J.A., 2010. Physical properties of a humic cambisol under tillage and cropping systems after 12 years. R. Bras. Ci. Solo 34, 219–226.

Assouline, S., Tessier, D., Bruand, A., 1998. A conceptual model of the soil water retention curve. Water Resour. Res. 34, 223–231.

Bacchi, O.O.S., Reichardt, K., Oliveira, J.C.M., Nielsen, D.R., 1998. Gamma-ray beam attenuation as an auxiliary technique for the evaluation of soil water retention curve. Sci. Agr. 55, 499–502.

Baumgartl, Th., 1998. Physical soil properties in specific fields of application especially in anthropogenic soils. Soil Till. Res. 47, 51–59.

Beckett, C.T.S., Augarde, C.E., 2013. Prediction of soil water retention properties using pore-size distribution and porosity. Can. Geotech. J. 50, 435–450.

Bodner, G., Scholl, P., Kaul, H.-P., 2013. Field quantification of wetting–drying cycles to predict temporal changes of soil pore size distribution. Soil Till. Res. 133, 1–9.

Borges, J.A.R., Pires, L.F., Cássaro, F.A.M., Roque, W.L., Heck, R.J., Rosa, J.A., Wolf, F.G., 2018. X-ray microtomography analysis of representative elementary volume (REV) of soil morphological and geometrical properties. Soil Till. Res. 182, 112–122.

580 Bouma, J., Jongerius, A., Boersma, O.H., Jager, A., Schoonderbeek, D., 1977.
581 The function of different types of macropores during saturated flow through
582 four swelling soil horizons. Soil Sci. Soc. Am. J. 41, 945–950.

583 Braudeau, E., Hovhannissian, G., Assi, A.T., Mohtar, R.H., 2014. Soil water
584 thermodynamic to unify water retention curve by pressure plates and
585 tensiometer. Front. Earth Sci. 2, Article 30.

586 Bresson, L.M., Moran, C.J., 2003. Role of compaction versus aggregate
587 disruption on slumping and shrinking of repacked hardsetting seedbeds. Soil
588 Sci. 168, 585–594.

589 Bruand, A., Cousin, I., 1995. Effect of water content on the fabric of a soil material:
590 An experimental approach. Eur. J. Soil Sci. 46, 377–385.

591 Cássaro, F.A.M., Posadas Durand, A.N., Gimenez, D., Vaz, C.M.P., 2017. Pore-
592 size distributions of soils derived using a geometrical approach and multiple
593 resolution MicroCT images. Soil Sci. Soc. Am. J. 81, 468–476.

594 Chen, R., Ng, C.W.W., 2013. Impact of wetting–drying cycles on hydro-
595 mechanical behavior of an unsaturated compacted clay. Appl. Clay Sci. 86,
596 38–46.

597 Czyż, E.A., Dexter, A.R., 2015. Mechanical dispersion of clay from soil into water:
598 readily-dispersed and spontaneously-dispersed clay. Inter. Agrophys. 29, 31-
599 37.

600 Dal Ferro, N., Charrier, P., Morari, F., 2014. Soil macro- and microstructure as
601 affected by different tillage systems and their effects on maize root growth. Soil
602 Till. Res. 140, 55–65.

603 Denef, K., Six, J., Paustian, K., Merckx, R., 2001a. Importance of
604 macroaggregate dynamics in controlling soil carbon stabilization: short-term
605 effects of physical disturbance induced by dry-wet cycles. Soil Biol. Bioch. 33,
606 2145–2153.

607 Denef, K., Six, J., Bossuyt, H., Frey, S.D., Elliot, E.T., Merckx, R., Paustian, K.,
608 2001b. Influence of dry-wet cycles on the interrelationship between aggregate,
609 particulate organic matter, and microbial community dynamics. Soil Biol.
610 Bioch. 33, 1599–1611.

611 Diel, J., Vogel, H.J., Schlüter, S., 2019. Impact of wetting and drying cycles on
612 soil structure dynamics. Geoderma 345, 63-71.

613 Dörner, J., Horn, R., 2006. Anisotropy of pore functions in structured Stagnic
614 Luvisols in the Weichselian moraine region in N Germany. J. Plant Nutrit. Soil
615 Sci. 169, 213–220.

616 Doube, M., Kłosowski, M.M., Arganda-Carreras, I., Cordelières, F.P., Dougherty,
617 R.P., Jackson, J.S., Schmid, B., Hutchinson, J.R., Shefelbine, S.J., 2010.
618 Bone 47, 1076–1079.

619 Ferreira, T.R., Pires, L.F., Wildenschild, D., Brinatti, A.M., Borges, J.A.R., Auler,
620 A.C., dos Reis, A.M.H., 2019. Lime application effects on soil aggregate
621 properties: Use of the mean weight diameter and synchrotron-based X-ray
622 µCT techniques. Geoderma 338, 585–596.

623 Galdos, M.V., Pires, L.F., Cooper, H.V., Calonego, J.C., Rosolem, C.A., Mooney,
624 S.J., 2019. Assessing the long-term effects of zero tillage on the macroporosity
625 of Brazilian soils using X-ray Computed Tomography. Geoderma 337, 1126–
626 1135.

627 Garbout, A., Munkholm, L.J., Hansen, S.B., 2013. Tillage effect on topsoil
628 structural quality assessed using X-ray CT soil cores and visual soil evaluation.
629 Soil Till. Res. 128, 104–109.

630 Ghezzehei, T.A., Or, D., 2000. Dynamics of soil aggregate coalescence governed
631 by capillary and rheological processes. Water Resour. Res. 36, 367–379.

632 He, Y., Cui, Y-J., Ye, W-M., Conil, N., 2017. Effects of wetting-drying cycles on
633 the air permeability of compacted Téguline clay. Eng. Geol. 228, 173–179.

634 Helliwell, J.R., Sturrock, C.J., Mairhofer, S., Craigon, J., Ashton, R.W., Miller,
635 A.J., Whalley, R., Mooney, S.J., 2017. The emergent rhizosphere: imaging the
636 development of the porous architecture at the root-soil interface. Scient.
637 Report. 7, 14875.

638 Hillel, D., 2004. Introduction to environmental soil physics. Elsevier Academic
639 Press, San Diego.

640 Hussein, J., Adey, M.A., 1995. Changes of structure and tilth mellowing in a
641 Vertisol due to wet/dry cycles in the liquid and vapour phases. Eur. J. Soil Sci.
642 46, 357–368.

643 Hussein, J., Adey, M.A., 1998. Changes in microstructure, voids and b-fabric of
644 surface samples of a Vertisol caused by wet/dry cycles. Geoderma 85, 63–82.

645 Jayanth, S., Iyer, K., Singh, D.N., 2012. Influence of drying and wetting cycles on
646 SWCCs of fine-grained soils. J. Test. Evaluat. 40, JTE104184.

647 Jefferies, D.A., Heck, R.J., Thevathasan, N. V., Gordon, A.M., 2014.
648 Characterizing soil surface structure in a temperate tree-based intercropping
649 system using X-ray computed tomography. Agrofor. Syst. 88, 645–656.

650 Jury, W.A., Horton, R., 2004. Soil Physics. Willey, New Jersey.

651 Katuwal, S., Norgaard, T., Moldrup, P., Lamandé, M., Wildenschild, D., de Jonge,
652 L.W., 2015. Linking air and water transport in intact soils to macropore
653 characteristics inferred from X-ray computed tomography. Geoderma 237/238,
654 9–20.

655 Klute, A., 1986. Water retention: laboratory methods. In: Black, C.A. (Ed.)
656 Methods of Soil Analysis. Part 1: Physical and Mineralogical Methods.
657 Madison, USA: Soil Science Society of America. pp. 635–662.

658 Kong, L., Sayem, H.Md., Tian, H., 2018. Influence of drying–wetting cycles on
659 soil-water characteristic curve of undisturbed granite residual soils and
660 microstructure mechanism by nuclear magnetic resonance (NMR) spin-spin
661 relaxation time (T2) relaxometry. Can. Geotech. J. 55, 208–216.

662 Kutílek, M., Nielsen, D.R., 1994. Soil Hydrology. Catena Verlag: Germany.

663 Lal, R., Shukla, M.K. 2004. Principles of soil physics. Marcel Dekker: New York,
664 USA.

665 Lee, T-K., Ro, H-M., 2014. Estimating soil water retention function from its
666 particle-size distribution. Geosci. J. 18, 219–230.

667 Leij, F.J., Ghezzehei, T.A., Or, D., 2002. Modeling the dynamics of the soil pore
668 size distribution. Soil Till. Res. 2002, 64, 61–78.

669 Li, D., Velde, B., Zhang, T., 2004. Observations of pores and aggregates during
670 aggregation in some clay-rich agricultural soils as seen in 2D image analysis.
671 Geoderma 118, 191–207.

672 Liu, Q., Yasufuku, N., Omine, K., Hazarika, H., 2012. Automatic soil water
673 retention test system with volume change measurement for sandy and silty
674 soils. Soils Found. 52, 368–380.

675 Luo, L., Lin, H., Li, S., 2010. Quantification of 3-D soil macropore networks in
676 different soil types and land uses using computed tomography. J. Hydrol. 393,
677 53–64.

678 Ma, R., Cai, C., Li, Z., Wang, J., Xiao, T., Peng, G., Yang, W., 2015. Evaluation
679 of soil aggregate microstructure and stability under wetting and drying cycles
680 in two Ultisols using synchrotron-based X-ray micro-computed tomography.
681 Soil Till. Res. 149, 1–11.

682 Marchuk, A., Rengasamy, P., McNeill, A., Kumar, A., 2012. Nature of the clay–
683 cation bond affects soil structure as verified by X-ray computed tomography.
684 Soil Res. 50, 638–644.

685 Moraes, S.O., Libardi, P.L., Dourado Neto, D., 1993. Problemas metodológicos
686 na obtenção da curva de retenção da água pelo solo. Sci. Agr. 50, 383–392
687 (in Portuguese, with English abstract).

688 Munkholm, L.J., Heck, R.J., Deen, B., 2012. Soil pore characteristics assessed
689 from X-ray micro-CT derived images and correlations to soil friability.
690 Geoderma 181/182, 22–29.

691 Ng, C.W.W., Pang, Y.W., 2000. Experimental investigations of the soil water
692 characteristics of a volcanic soil. Can. Geotech. J. 37:1252–1264.

693 Oades, J.M., 1984. Soil organic matter and structural stability: mechanisms and
694 implications for management. Plant Soil 76, 319–337.

695 Otsu, N., 1979. A threshold selection method from gray-level histograms. IEEE
696 Transactions on Systems, Man and Cybernetics l. SMC-9, 62–6.

697 Pagliai, M., La Marca, M., Lucamante, G., 1987. Changes in soil porosity in
698 remolded soils treated with poultry manure. Soil Science 144, 128–140.

699 Pagliai, M., Vignozzi, N., 2002. The soil pore system as an indicator of soil quality.
700 Advances in GeoEcology 35, 69-80.

701 Pardini, G., Vigna Guidi, G., Pini, R., Regüés, D., Gallart, F., 1996. Structure and
702 porosity of smectitic mudrocks as affected by experimental wetting-drying
703 cycles and freezing-thawing cycles. Catena 27, 149–165.

704 Peng, X., Horn, R., Smucker, A., 2007. Pore shrinkage dependency of inorganic
705 and organic soils on wetting and drying cycles. Soil Sci. Soc. Am. J. 71, 1095–
706 1104.

707 Périard, Y., José Gumiere, S., Long, B., Rousseau, A.N., Caron, J., 2016. Use of
708 X-ray CT scan to characterize the evolution of the hydraulic properties of a soil
709 under drainage conditions. Geoderma 279, 22–30.

710 Peth, S., Horn, R., Beckmann, F., Donath, T., Fischer, J., Smucker, A.J.M., 2008.
711 Three-dimensional quantification of intra-aggregate pore-space features using
712 synchrotron-radiation-based microtomography. Soil Sci. Soc. Am. J. 72, 897–
713 907.

714 Petrovic, A.M., Siebert, J.E., Rieke, P.E., 1982. Soil bulk density analysis in three
715 dimensions by computed tomographic scanning. Soil Sci. Soc. Am. J. 46, 445–
716 450.

717 Piccoli, I., Camarotto, C., Lazzaro, B., Furlan, L., Morari, F., 2017. Conservation
718 Agriculture Had a Poor Impact on the Soil Porosity of Veneto Low-lying Plain

719 Silty Soils after a 5-year Transition Period. Land Degrad. Develop. 28, 2039-
720 2050.

721 Piccoli, I., Schjønning, P., Lamandé, M., Zanini, F., Morari, F., 2019. Coupling
722 gas transport measurements and X-ray tomography scans for multiscale
723 analysis in silty soils. Geoderma 338, 576-584.

724 Pires, L.F., Bacchi, O.O.S., Reichardt, K., 2005. Gamma ray computed
725 tomography to evaluate wetting/drying soil structure changes. Nucl. Inst. Meth.
726 Phys. Res. 229, 443–456.

727 Pires, L.F., Borges, J.A.R., Rosa, J.A., Cooper, M., Heck, R., Passoni, S., Roque,
728 W.L., 2017. Soil structure changes induced by tillage systems. Soil Till. Res.
729 165, 66–79.

730 Pires, L.F., Cássaro, F.A.M., Reichardt, K., Bacchi, O.O.S. 2008a. Soil porous
731 system changes quantified by analyzing soil water retention curve
732 modifications. Soil Till. Res. 100, 72–77.

733 Pires, L.F., Cooper, M., Cássaro, F.A.M., Reichardt, K., Bacchi, O.O.S., Dias,
734 N.M.P., 2008b. Micromorphological analysis to characterize structure
735 modifications of soil samples submitted to wetting and drying cycles. Catena
736 72, 297–304.

737 Pires, L.F., Mooney, S.J., Auler, A.C., Atkinson, B., Sturrock, C.J., 2019. X-ray
738 microtomography to evaluate the efficacy of paraffin wax coating for soil bulk
739 density evaluation. Geoderma 337, 935–944.

740 Pires, L.F., Villanueva, F.C.A., Dias, N.M.P., Bacchi, O.O.S., Reichardt, K., 2011.
741 Chemical migration during soil water retention curve evaluation. An. Braz.
742 Acad. Sci. 83, 1097–1107.

743 R Core Team, 2018. R: A Language and Environment for Statistical Computing.
744 R Foundation for Statistical Computing, Vienna.

745 Radcliffe, D.E., Simùnek, J., 2010. Soil physics with Hydrus: Modelling and
746 applications. CRC Press, Boca Raton, USA.

747 Rafraf, S., Guellouz, L., Guiras, H., Bouhlila, R., 2016. Quantification of hysteresis
748 effects on a soil subjected to drying and wetting cycles. Int. Agrophys. 30, 493–
749 499.

750 Rajaram, G., Erbach, D.C., 1999. Effect of wetting and drying on soil physical
751 properties. J. Terramechanics 36, 39–49.

752 Rasa, K., Eickhorst, T., Tippkötter, R., Yli-Halla, M., 2012. Structure and pore
753 system in differently managed clayey surface soil as described by
754 micromorphology and image analysis. Geoderma 173-174, 10–18.

755 Rasband, W., 2007. ImageJ.1997–2007. U.S.National Institutes of Health,
756 Bethesda, MD, USA.

757 Reis, A. M. H., Armindo, R., Pires, L., 2019. Physical assessment of a
758 Haplohumox soil under integrated crop-livestock system. Soil Till. Res. 194,
759 104294.

760 Reynolds, W.D., Topp, G.C., 2006. Soil Water Desorption and Imbibition: Tension
761 and Pressure Techniques. In: Carter, M.R., Gregorich, E.G. Soil sampling and
762 methods of analysis. 2nd ed. Boca Raton: CRC Press. pp. 981-998

763 Romano, N., Hopmans, J.W., Dane, J.H., 2002. Suction table. In: Dane. J.H.,
764 Topp, G.C. (Eds.). Methods of Soil Analysis. Part 4: Physical Methods.
765 Madison, USA: Soil Science Society of America. pp. 692-698.

766 Roque, W.L., Arcaro, K., Lanfredi, R.B., 2012. Trabecular network tortuosity and
767 connectivity of distal radius from microtomographic images. Brazilian J.
768 Biomed. Eng. 28, 116–123.

769 Roque, W.L., Souza, A.C.A. de, Barbieri, D.X., 2009. The Euler-Poincaré
770 characteristic applied to identify low bone density from vertebral tomographic
771 images. Rev. Bras. Reumatol. 49, 140–152.

772 Sartori, G., Ferrari, G.A., Pagliai, M., 1985. Changes in soil porosity and surface
773 shrinkage in a remolded, saline clay soil treated with compost. Soil Sci. 139,
774 523–530.

775 Sayem, H.M., Kong, L., 2016. Effects of drying-wetting cycles on soil-water
776 characteristic curve. 2016 International Conference on Power Engineering &
777 Energy, Environment (PEEE 2016).

778 Schlüter, S., Leuther, F., Vogler, S., Vogel, H.-J., 2016. X-ray microtomography
779 analysis of soil structure deformation caused by centrifugation. Solid Earth 7,
780 129–140.

781 Smagin, A.V., 2012. Column-centrifugation method for determining water
782 retention curves of soils and disperse sediments. Eur. Soil Sci. 45, 416–422.

783 Smet, S., Plougonven, E., Leonard, A., Degré, A., Beckers, E., 2017. X-ray Micro-
784 CT: How soil pore space description can be altered by image processing.
785 Vadose Zone J. EI, 2–14.

786 Soil Survey Staff, 2013. Simplified guide to soil taxonomy. USDA-Natural
787 Resources Conservation Service, National Soil Survey Center, Lincoln, USA.

788 Stange, C.F., Horn, R., 2005. Modeling the soil water retention curve for
789 conditions of variable porosity. Vad. Zone J. 4, 602–613.

790 Tang, C.S., Shi, B., 2011. Swelling and shrinkage behaviour of expansive soil
791 during wetting–drying cycles. Chin. J. Geotech. Eng. 33 (9), 1376–1384.

792 Tessier, D., Beaumont, A., Pedro, G., 1990. Influence of clay mineralogy and
793 rewetting rate on clay microstructure. In: Douglas, L.A. (Ed.). Soil
794 micromorphology. Amsterdam: Elsevier Science Publisher, 1990. pp. 115–
795 121.

796 Thurston, W.P., 1997. Three-dimensional Geometry and Topology, 1st ed.
797 Princeton University Press, Princeton.

798 Tracy, S.R., Daly, K.R., Sturrock, C., Crout, N.M.J., Mooney, S.J., Roose, T.,
799 2015. Three-dimensional quantification of soil hydraulic properties using X-ray
800 Computed Tomography and image-based modeling. Water Resour. Res. 51,
801 1006–1022.

802 Van Genuchten, M.Th., 1980. A closed-form equation for predicting the hydraulic
803 conductivity of unsaturated soils. Soil Sci. Soc. Am. J. 44, 892–898.

804 Vandenbygaard, A.J., Protz, R., Tomlin, A.D., 1999. Changes in pore structure in
805 a no-till chronosequense of silt loam soils, Southern Ontario. Can. J. Soil Sci.
806 79, 149–160.

807 Vasconcelos do Nascimento, I., Leite de Alencar, T., Anastácio dos Santos, C.L.,
808 Assis Júnior, R.N., Mota, J.C.A., 2018. Effect of sample re-saturation on soil-
809 water characteristic curve. Caatinga 31, 446–454.

810 Vogel, H.J., Roth, K., 2001. Quantitative morphology and network representation
811 of soil pore structure. Adv. Water Resour. 24, 233–242.

812 Vogel, H.J., Weller, U., Schluter, S., 2010. Quantification of soil structure based
813 on Minkowski functions. Comput. Geosci. 36, 1236–1245.

814 Yoon, Y., Kim, J.G., Hyun, S., 2007. Estimating soil water retention in a selected
815 range of soil pores using tension disc infiltrometer data. Soil Till. Res. 97, 107-
816 116.

817 Zemenu, G., Martine, A., Roger, C., 2009. Analysis of the behaviour of a natural
818 expansive soil under cyclic drying and wetting. Bull. Eng. Geol. Environ. 68,
819 421–436.

820 Zhang, M., Lu, Y., Heitman, J., Horton, R., Ren, T., 2018. Temporal changes of
821 soil water retention behavior as affected by wetting and drying following tillage.
822 Soil Sci. Soc. Am. J. 81, 1288–1295.

823 Zhang, X., Mavroulidou, M., Gunn, M.J., 2017. A study of the water retention
824 curve of lime-treated London Clay. Acta Geot. 12, 23–45.

825 Zhang, Z.B., Zhou, H., Zhao, Q.G., Lin, H., Peng, X., 2014. Characteristics of
826 cracks in two paddy soils and their impacts on preferential flow. Geoderma
827 228, 114–121.

828 Zhou H., Mooney, S.J., Peng, X.H., 2017. Bimodal pore structure investigated by
829 a combined SWRC and X-ray Computed Tomography approach. Soil Sci. Soc.
830 Am. J. 81, 1270–1278.

831 Zingg, T., 1935. Beitrag zur Schotteranalyse. Schweiz. Mineral. Petrogr. Mitt., 15,
832 39–140.

833

Table Captions

Table 1. Pearson's correlation coefficients between the morphological properties of the soil porous architecture for the whole region of interest (ROI_W) and the region of interest close to bottom of the sample (ROI_{HC}).

Table 2. Soil water retention curve (SWRC) parameters from the van Genuchten (1980) mathematical model before (0) and after the application of 6 and 12 wetting and drying (W-D) cycles.

Table 3. Pearson's correlation coefficients between the morphological attributes of the soil porous architecture for the whole region of interest (ROI_W) and soil water retention curve (SWRC) parameters based on the van Genuchten (1980) mathematical model.

Figure Captions

Fig. 1. 3D visualization of the soil samples under zero tillage before (0) and after the application of 6 and 12 wetting and drying (W-D) cycles. ROI_W: whole region of interest. ROI_{HC}: region of interest close to the bottom of the sample.

Fig. 2. Morphological parameters of the soil porous system before (0) and after the application of 6 and 12 wetting and drying (W-D) cycles: (a) Porosity (P); (b) Number of Pores (NP); (c) Degree of anisotropy (DA); (d) Connectivity (EPC/V); (e) Number of junctions (N_{junc}); (f) Number of branches (N_{branch}). ROI_W (▭): whole region of interest. ROI_{HC} (▬): region of interest close to the bottom of the sample. Means followed by the same upper case letters between ROI_W and ROI_{HC} and same lowercase between W-D cycles did not differ from each other by t-Student test ($p \leq 0.05$). n=3 (number of samples analyzed for each treatment).

Fig. 3. Average tortuosity (τ) (a); tortuosity in the x-directions (b); tortuosity in the y-direction (c); tortuosity in the z-direction (d) of soil pores before (0) and after the application of 6 and 12 wetting and drying (W-D) cycles. ROI_W (▭): whole region of interest. ROI_{HC} (▬): region of interest close to the bottom of the sample. Means followed by the same upper case letters between ROI_W and ROI_{HC} and same lowercase between W-D cycles did not differ from each other by t-Student test ($p \leq 0.05$). n=3 (number of samples analyzed for each treatment).

Fig. 4. Pore size distribution based on volume before (0) and after the application of 6 and 12 wetting and drying (W-D) cycles: (a) Volume of pores (VP) between 0.0001 to 0.01 mm^3 ($VP_{0.0001-0.01}$); (b) VP between 0.01 to 0.1 mm^3 ($VP_{0.01-0.1}$); (c) Volume of pores between 0.1 to 1 mm^3 ($VP_{0.1-1}$). (d) VP between 1 to 10 mm^3 (VP_{1-10}); (e) VP >10 mm^3 ($VP_{>10}$). ROI_W (▭

): whole region of interest. ROI_{HC} (▬): region of interest close to the bottom of the sample. Means followed by the same upper case letters between ROI_W and ROI_{HC} and same lowercase between W-D cycles did not differ from each other by t-Student test ($p \leq 0.05$). n=3 (number of samples analyzed for each treatment).

Fig. 5. Pore distribution based on shape before (0) and after the application of 6 and 12 wetting and drying (W-D) cycles: (a) Equant shaped volume of pores (VP_{Eq}); (b) Prolate shaped volume of pores (VP_{Pr}); (c) Oblate shaped volume of pores (VP_{Ob}); (d) Triaxial shaped volume of pores (VP_{Tr}). ROI_W (▭): whole region of interest. ROI_{HC} (▬): region of interest close to the bottom of the sample. Means followed by the same upper case letters between ROI_W and ROI_{HC} and same lowercase between W-D cycles did not differ from each other by t-Student test ($p \leq 0.05$). n=3 (number of samples analyzed for each treatment).

Fig. 6. Water retention curve (SWRC) (a); SWRC relative differences (b) as function of the equivalent cylindrical diameter (D) of the pores before (0) and after the application of 6 and 12 wetting and drying (W-D) cycles. VG: van Genuchten mathematical model. Exp: Experimental data. The capillary rise equation was utilized to convert pressure heads in pore sizes. n=6 (number of samples analyzed for each treatment).

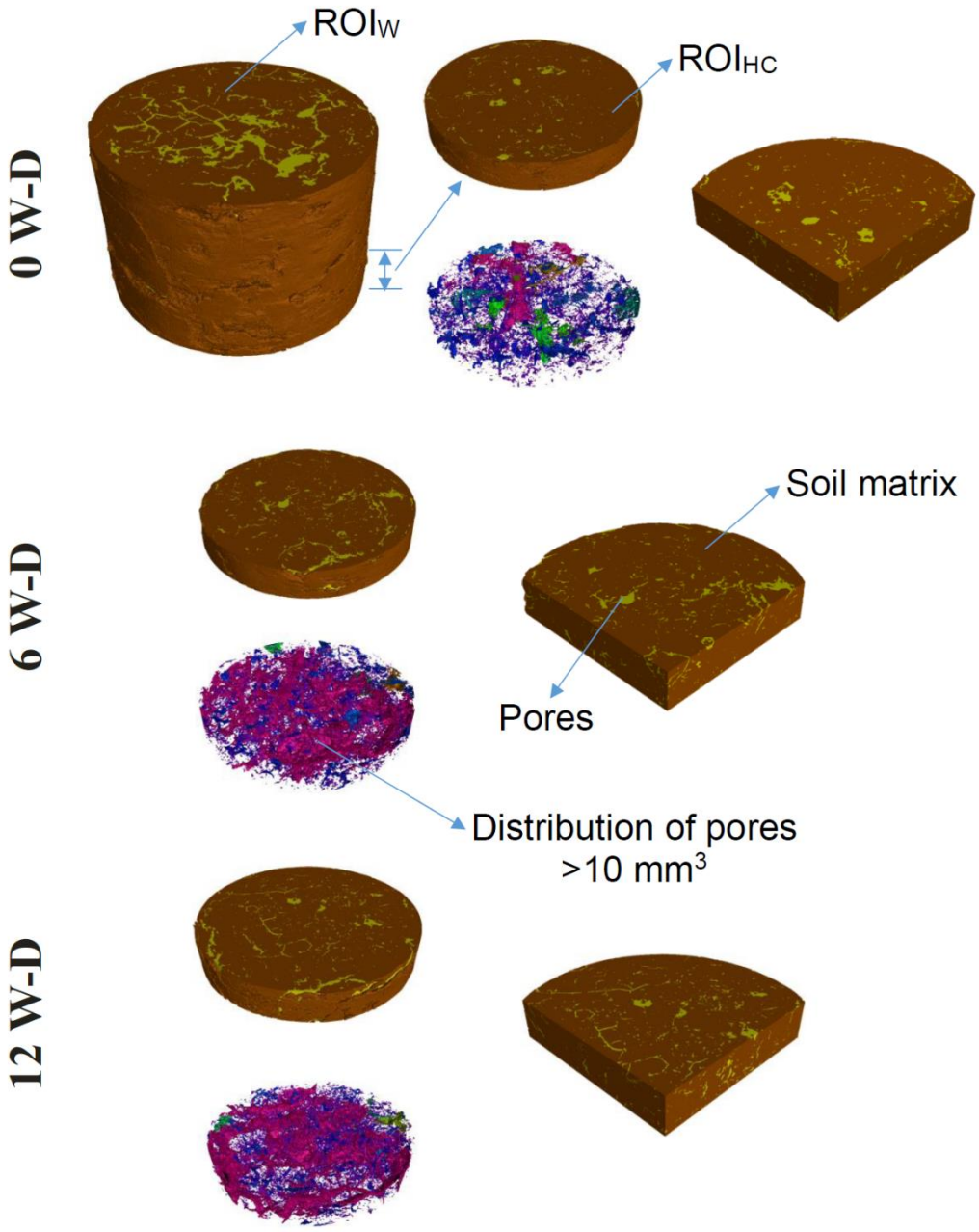
ROIW
ROIHC
0 W-D
6 W-D
12 W-D
Soil matrix
Pores
Distribution of pores
>10 mm3

Fig 1.

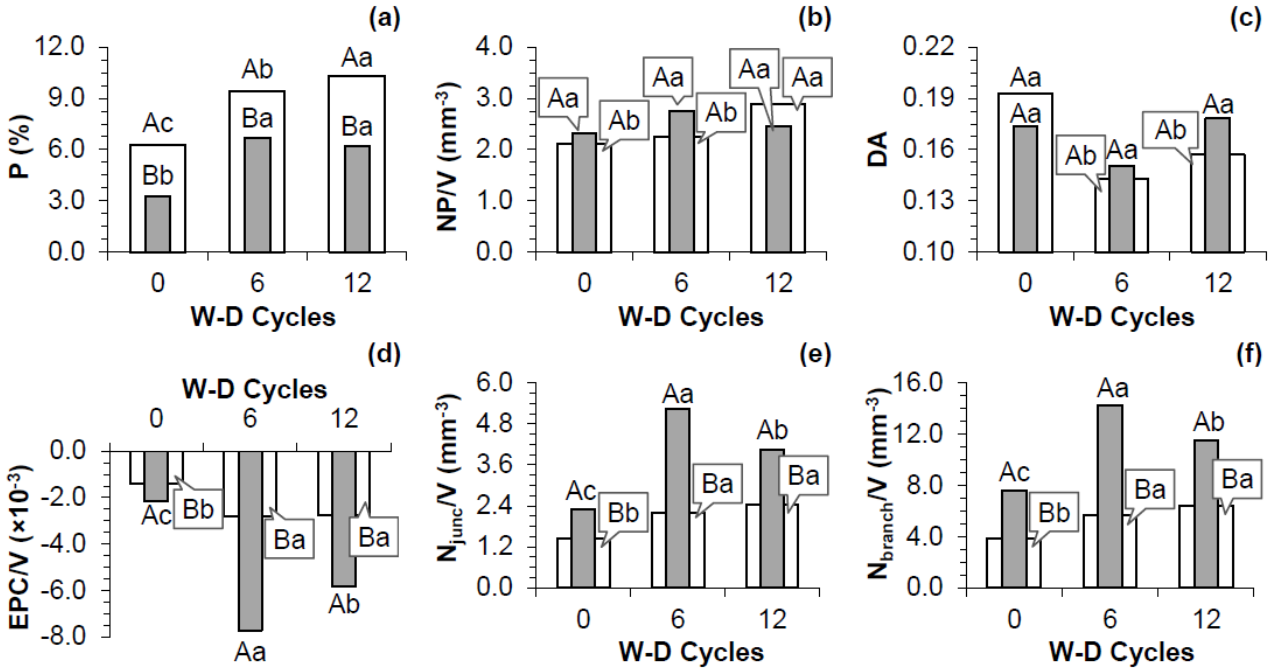
(a)
P (%)
12.0
9.0
6.0
3.0
0.0
Ac
Bb
Ab
Ba
Aa
Ba
0
6
12
W-D Cycles
(b)
NP/V (mm-3)
4.0
3.0
2.0
1.0
0.0
Aa
Ab
Aa
Ab
Aa
Aa
0
6
12
W-D Cycles
(c)
DA
0.22
0.19
0.16
0.13
0.10
Aa
Aa
Ab
Aa
Ab
Aa
0
6
12
W-D Cycles
(d)
W-D Cycles
0
6
12
EPC/V (×10-3)
0.0
-2.0
-4.0
-6.0
-8.0
Ac
Bb
Ba
Aa
Ba
Ab
(e)
Njunc/V (mm-3)
6.0
4.8
3.6
2.4
1.2
0.0
Ac
Bb
Aa
Ba
Ab
Ba
0
6
12
W-D Cycles
(f)
Nbranch/V (mm-3)
16.0
12.0
8.0
4.0
0.0
Ac
Bb
Aa
Ba
Ab
Ba
0
6
12
W-D Cycles

Fig 2.

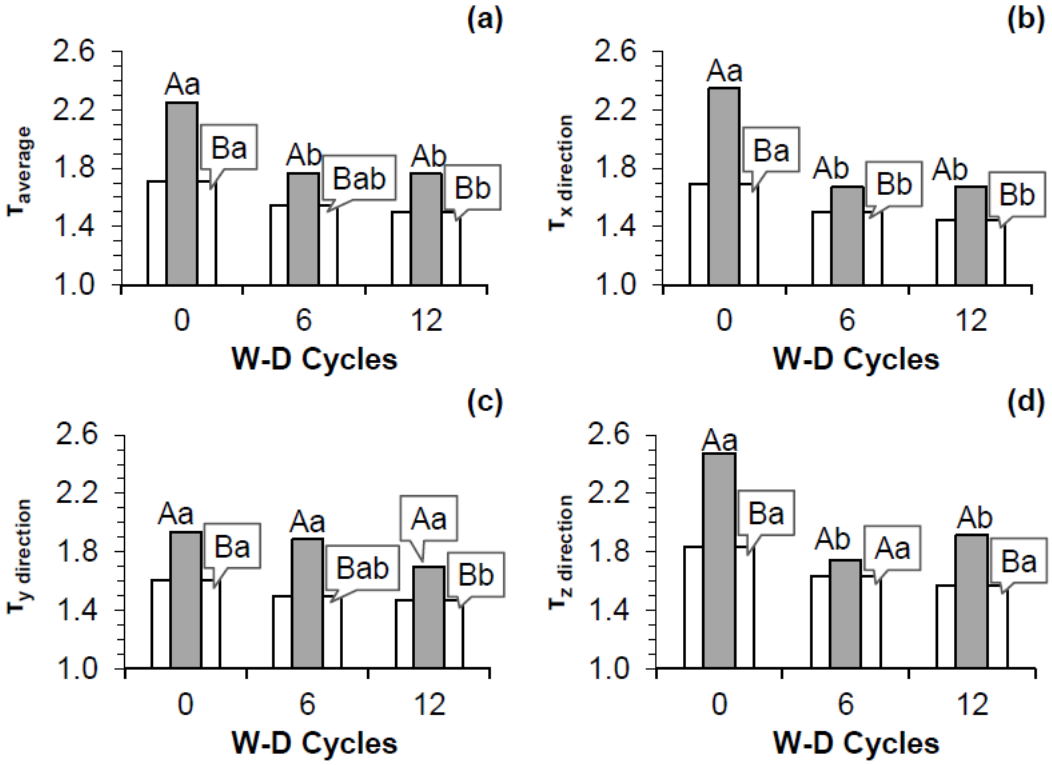
(a)
(b)
(c)
(d)
$T_{average}$
$T_{x\ direction}$
$T_{y\ direction}$
$T_{z\ direction}$
2.6
2.2
1.8
1.4
1.0
0
6
12
W-D Cycles
Aa
Ba
Ab
Bab
Bb

Fig 3.

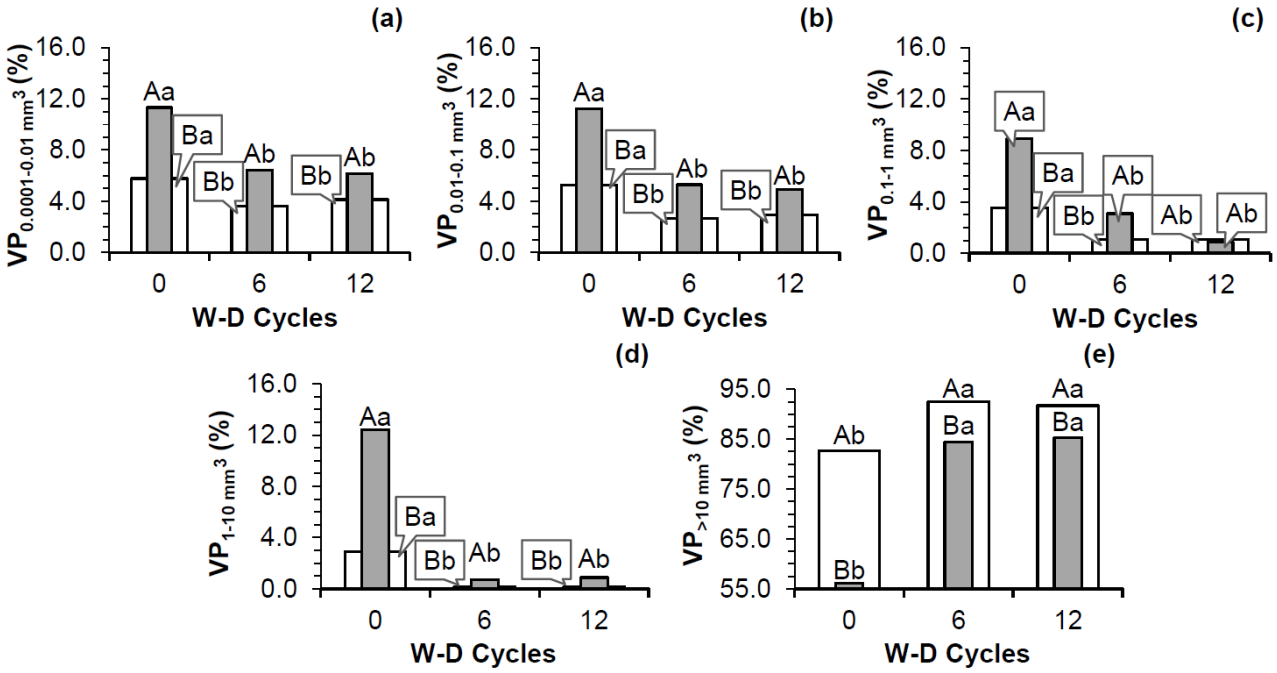
(a)
(b)
(c)
(d)
(e)
$VP_{0.0001\text{-}0.01\ mm^3}$ (%)
$VP_{0.01\text{-}0.1\ mm^3}$ (%)
$VP_{0.1\text{-}1\ mm^3}$ (%)
$VP_{1\text{-}10\ mm^3}$ (%)
$VP_{>10\ mm^3}$ (%)
W-D Cycles
Aa
Ba
Ab
Bb

Fig 4.

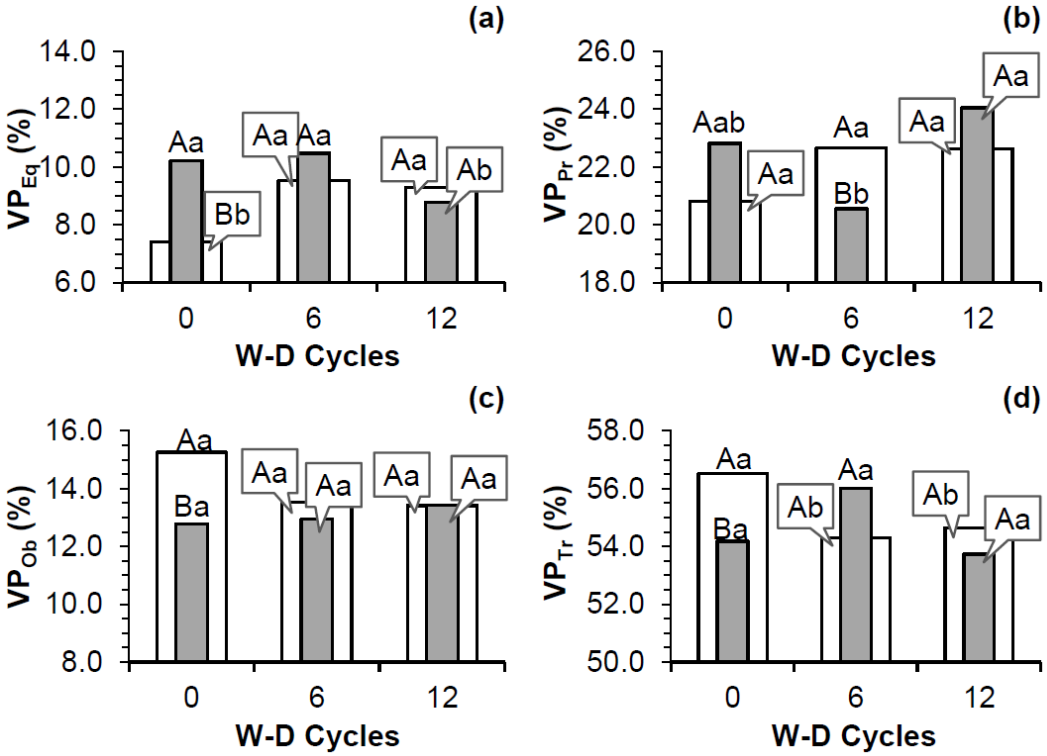
(a)
14.0
12.0
10.0
8.0
6.0
VPEq (%)
Aa
Bb
Aa
Aa
Aa
Ab
0
6
12
W-D Cycles
(b)
26.0
24.0
22.0
20.0
18.0
VPPr (%)
Aab
Aa
Aa
Bb
Aa
Aa
0
6
12
W-D Cycles
(c)
16.0
14.0
12.0
10.0
8.0
VPOb (%)
Aa
Ba
Aa
Aa
Aa
Aa
0
6
12
W-D Cycles
(d)
58.0
56.0
54.0
52.0
50.0
VPTr (%)
Aa
Ba
Ab
Aa
Ab
Aa
0
6
12
W-D Cycles

Fig 5.

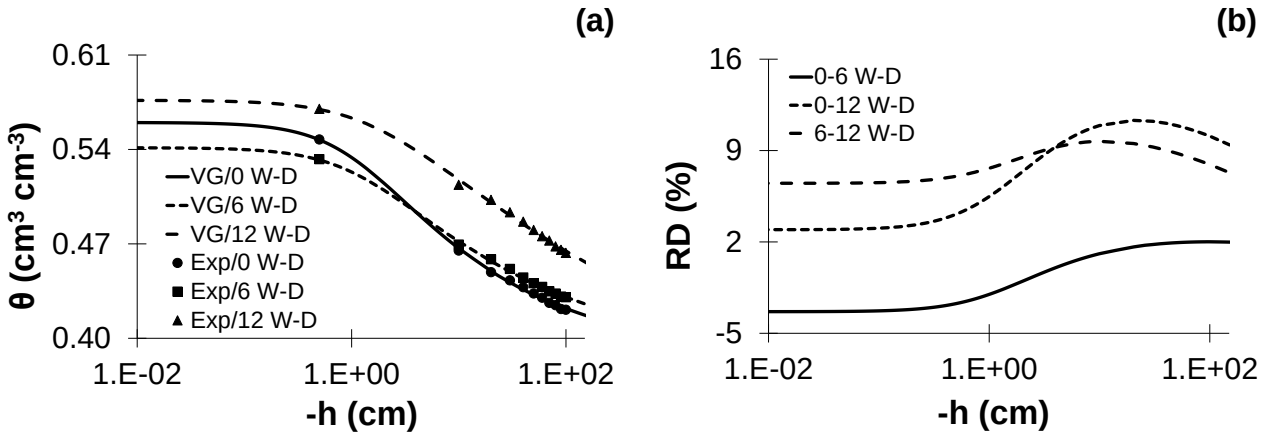
(a)
0.61
0.54
0.47
0.40
θ (cm³ cm⁻³)
VG/0 W-D
VG/6 W-D
VG/12 W-D
Exp/0 W-D
Exp/6 W-D
Exp/12 W-D
1.E-02
1.E+00
1.E+02
-h (cm)
(b)
16
9
2
-5
RD (%)
0-6 W-D
0-12 W-D
6-12 W-D
1.E-02
1.E+00
1.E+02
-h (cm)

Fig 6.

Table 1.

Variables	ROI_{HC}									
	P	**NP/V**	**DA**	**EPC/V**	**N_{junc}/V**	**N_{branch}/V**	**$\tau_{average}$**	**$\tau_{x\ direction}$**	**$\tau_{y\ direction}$**	**$\tau_{z\ direction}$**
Morphological properties										
P	1.00									
NP/V	0.44	1.00								
DA	-0.17	**-0.80***	1.00							
EPC/V	**-0.95***	-0.51	0.32	1.00						
N_{junc}/V	**0.92***	0.44	-0.24	**-0.98***	1.00					
N_{branch}/V	**0.95***	0.57	-0.35	**-0.98***	**0.97***	1.00				
$\tau_{average}$	**-0.91***	-0.34	0.07	**0.87***	**-0.83***	**-0.33***	1.00			
$\tau_{x\ direction}$	**-0.95***	-0.41	0.13	**0.87***	**-0.83***	**-0.86***	**0.98***	1.00		
$\tau_{y\ direction}$	-0.46	-0.01	-0.43	0.24	-0.18	-0.28	0.59	**0.63***	1.00	
$\tau_{z\ direction}$	**-0.86**	-0.60	0.32	**0.90***	**-0.87***	**-0.88***	**0.90***	**0.91***	0.40	1.00
Pore size distribution										
$VP_{0.0001\text{-}0.01\ mm^3}$	**-0.96***	-0.33	0.08	**0.90***	**-0.88***	**-0.86***	**0.95***	**0.96***	0.49	**0.87***
$VP_{0.01\text{-}0.1\ mm^3}$	**-0.96***	-0.40	0.16	**0.91***	**-0.88***	**-0.87***	**0.95***	**0.96***	0.48	**0.90***
$VP_{0.1\text{-}1\ mm^3}$	**-0.97***	-0.38	0.13	**0.91***	**-0.88***	**-0.88***	**0.90***	**0.93***	0.46	**0.84***
$VP_{1\text{-}10\ mm^3}$	**-0.95***	-0.46	0.20	**0.94***	**-0.91***	**-0.89***	**0.89***	**0.90***	0.36	**0.89***
$VP_{>10\ mm^3}$	**0.96***	0.36	-0.09	**-0.92***	**0.90***	**0.89***	**-0.90***	**-0.92***	-0.45	**-0.87***
Pore shape distribution										
VP_{Eq}	-0.24	0.01	-0.07	-0.02	0.06	0.02	0.29	0.37	0.51	0.09
VP_{Pr}	-0.25	-0.26	0.39	0.45	-0.47	-0.48	0.04	0.02	-0.48	0.12
VP_{Ob}	0.31	-0.38	0.54	-0.15	0.12	0.11	-0.47	-0.39	-0.56	-0.10
VP_{Tr}	0.31	**0.80***	**-0.83***	-0.33	0.30	0.44	-0.11	-0.24	0.15	-0.29

	ROI_{W}									
	P	**NP/V**	**DA**	**EPC/V**	**N_{junc}/V**	**N_{branch}/V**	**$\tau_{average}$**	**$\tau_{x\ direction}$**	**$\tau_{y\ direction}$**	**$\tau_{z\ direction}$**
Morphological attributes										
P	1.00									
NP/V	0.60	1.00								
DA	**-0.77***	-0.50	1.00							
EPC/V	**-0.92***	-0.46	**0.84***	1.00						
N_{junc}/V	**0.86***	**0.66***	**-0.80***	**-0.89***	1.00					
N_{branch}/V	**0.91***	0.62	**-0.74***	**-0.87***	**0.95***	1.00				
$\tau_{average}$	**-0.75***	**-0.79***	**0.75***	**0.71***	**-0.67***	**-0.67***	1.00			
$\tau_{x\ direction}$	**-0.85***	**-0.73***	**0.81***	**0.89***	**-0.90***	**-0.86***	**0.89***	1.00		
$\tau_{y\ direction}$	**-0.70***	**-0.69***	**0.69***	0.63	-0.60	-0.59	**0.87***	**0.79***	1.00	
$\tau_{z\ direction}$	**-0.74***	**-0.77***	**0.72***	**0.67***	-0.59	-0.55	**0.94***	**0.81***	**0.81***	1.00
Pore size distribution										
$VP_{0.0001\text{-}0.01\ mm^3}$	**-0.85***	-0.38	**0.80***	**0.94***	**-0.71***	**-0.71***	**0.77***	**0.84***	**0.69***	**0.74***
$VP_{0.01\text{-}0.1\ mm^3}$	**-0.88***	-0.51	**0.81***	**0.90***	**-0.74***	**-0.76***	**0.84***	**0.88***	**0.85***	**0.77***
$VP_{0.1\text{-}1\ mm^3}$	**-0.95***	-0.59	**0.88***	**0.98***	**-0.88***	**-0.88***	**0.81***	**0.92***	**0.75***	**0.77***
$VP_{1\text{-}10\ mm^3}$	**-0.96***	-0.55	**0.88***	**0.98***	**-0.89***	**-0.89***	**0.75***	**0.88***	**0.69***	**0.73***
$VP_{>10\ mm^3}$	**0.90***	0.57	**-0.87***	**-0.86***	**0.72***	**0.77***	**-0.88***	**-0.84***	**-0.82***	**-0.85***
Pore shape distribution										
VP_{Eq}	**0.80***	0.53	**-0.83***	**-0.78***	**0.71***	**0.74***	**-0.82***	**-0.82***	**-0.92***	**-0.71***
VP_{Pr}	**0.76***	0.39	-0.60	-0.61	0.45	0.62	**-0.73***	-0.60	**-0.74***	-0.64
VP_{Ob}	**0.70***	-0.28	0.52	0.54	-0.46	**-0.67***	0.56	0.51	0.62	0.40
VP_{Tr}	-0.61	-0.35	0.58	**0.70***	-0.58	-0.47	0.52	**0.65***	**0.74***	0.54

P = Porosity by image; NP = Number of Pores; DA = Degree of anisotropy; EPC/V = Connectivity (EPC/V); N_{junc} = Number of junctions; N_{branch} = Number of branches; $\tau_{average}$ = Average tortuosity; τ_x. τ_y and τ_z = tortuosity in the directions x. y and z. respectively; $VP_{0.0001\text{-}0.01\ mm^3}$, $VP_{0.01\text{-}0.1\ mm^3}$, $VP_{0.1\text{-}1\ mm^3}$, $VP_{1\text{-}10\ mm^3}$ and $VP_{>10\ mm^3}$ = Volume of pores between 0.0001 to 0.01 mm^3, 0.01 to 0.1 mm^3, 0.1 to 1 mm^3, 1 to 10 mm^3 and >10 mm^3, respectively; VP_{Eq}, VP_{Pr}, VP_{Ob} and VP_{Tr} = Volume of equant, prolate, oblate and triaxial shaped pores. *$p \leq 0.05$. n=3 (number of samples analyzed for each treatment).

Table 2.

W-D cycles	θ_s	θ_r	α	n	m	R^2
	$cm^3\ cm^{-3}$		cm^{-1}			
0	0.560	0.382	0.914	1.329	0.248	0.99
6	0.541	0.378	0.812	1.258	0.205	0.99
12	0.576	0.307	0.579	1.132	0.117	0.99

n=6 (number of samples analyzed for each treatment).

Table 3.

Porous properties	Van Genuchten (1980) parameters			
	θ_s	θ_r	α	n
Morphological properties				
P	0.16	**-0.69***	**-0.84***	**-0.87***
NP/V	0.58	**-0.80***	**-0.80***	**-0.79***
DA	0.28	0.26	0.47	0.51
EPC/V	0.10	-0.48	**0.68***	**0.73***
N_{junc}/V	0.16	-0.65*	**-0.79***	**-0.82***
N_{branch}/V	0.23	-0.71*	**-0.83***	**-0.85***
$T_{average}$	-0.12	0.53	0.64	**0.66***
$T_{x\ direction}$	-0.14	0.62	**0.76***	**0.79***
$T_{y\ direction}$	-0.09	0.47	0.58	0.61
$T_{z\ direction}$	-0.13	0.53	0.64	**0.66***
Pore size distribution				
$VP_{0.0001\text{-}0.01\ mm^3}$	0.25	0.32	0.53	0.57
$VP_{0.01\text{-}0.1\ mm^3}$	0.13	0.42	0.61	**0.65***
$VP_{0.1\text{-}1\ mm^3}$	0.05	0.53	**0.72***	**0.76***
$VP_{1\text{-}10\ mm^3}$	0.05	0.54	**0.73***	**0.77***
$VP_{>10\ mm^3}$	-0.11	-0.43	-0.62	**-0.66***
Pore shape distribution				
VP_{Eq}	-0.12	-0.37	-0.54	-0.58
VP_{Pr}	-0.03	0.35	0.48	-0.51
VP_{Ob}	-0.01	0.34	0.45	0.47
VP_{Tr}	0.14	0.29	0.46	0.49

P = Porosity; NP = Number of Pores; DA = Degree of anisotropy; EPC/V = Connectivity (EPC/V); N_{junc} = Number of junctions; N_{branch} = Number of branches; $\tau_{average}$ = Average tortuosity; τ_x. τ_y and τ_z = tortuosity in the directions x. y and z. respectively; $VP_{0.0001\text{-}0.01\ mm^3}$, $VP_{0.01\text{-}0.1\ mm^3}$, $VP_{0.1\text{-}1\ mm^3}$, $VP_{1\text{-}10\ mm^3}$ and $VP_{>10\ mm^3}$ = Volume of pores between 0.0001 to 0.01 mm^3, 0.01 to 0.1 mm^3, 0.1 to 1 mm^3, 1 to 10 mm^3 and >10 mm^3, respectively; VP_{Eq}, VP_{Pr}, VP_{Ob} and VP_{Tr} = Volume of equant, prolate, oblate and triaxial shaped pores. *p≤0.05. n = 3 (number of samples analyzed for each treatment for computed tomographic analysis). n=6 (number of samples analyzed for each treatment for soil water retention curve).

SUPPLEMENTARY TABLE

(to be included as supplementary material)

Table A. Summary of the statistical analysis [t–value. variance (σ^2) and probability (*p*)] performed on the morphological properties of soil pores obtained by microtomography. Samples were submitted to 0. 6 and 12 wetting and drying (W-D) cycles. Two regions of interest were selected for the image analysis: whole sample (ROI_W) and region close to the hydraulic contact (ROI_{HC}) with the sandbox

Properties analyzed	Statistics	Orthogonal contrasts analyzed								
		ROI_W × ROI_{HC} in each W-D cycle			Between W-D cycles in ROI_W			Between W-D cycles in ROI_{HC}		
		0 W-D	6 W-D	12 W-D	0 × 6 W-D	0 × 12 W-D	6 × 12 W-D	0 × 6 W-D	0 × 12 W-D	6 × 12 W-D
Morphological attributes										
P (%)	t-value	9.503	7.627	10.048	-9.621	-10.924	-2.837	-9.827	-8.250	1.058
	σ^2	0.155	0.193	0.249	0.161	0.206	0.150	0.187	0.198	0.292
	p	**0.001**	**0.002**	**<0.001**	**<0.001**	**<0.001**	**0.024**	**0.001**	**0.002**	0.175
NP/V	t-value	-0.836	-1.790	1.931	-0.609	-3.122	-2.586	0.119	0.075	0.098
	σ^2	0.097	0.115	0.069	0.092	0.091	0.085	-1.538	-0.634	1.140
	p	0.225	0.074	0.063	0.288	**0.018**	**0.030**	0.099	0.280	0.169
DA	t-value	2.107	-0.512	-1.166	5.216	3.178	-1.467	1.558	-0.292	-1.301
	σ^2	$1.311\ 10^{-4}$	$3.36\ 10^{-4}$	$5.01\ 10^{-4}$	$1.40\ 10^{-4}$	$1.92\ 10^{-4}$	$1.43\ 10^{-4}$	$3.27\ 10^{-4}$	$4.40\ 10^{-4}$	$6.95\ 10^{-4}$
	p	0.063	0.322	0.164	**0.003**	**0.017**	0.108	0.130	0.399	0.132
EPC/V	t-value	3.775	20.252	31.478	10.172	9.034	-1.078	20.140	23.030	-7.584
	σ^2	0.056	0.087	0.015	0.029	0.032	0.010	0.115	0.039	0.092
	p	**0.010**	**0.001**	**<0.001**	**0.001**	**0.001**	0.171	**<0.001**	**<0.001**	0.008
N_{junc}/V	t-value	-5.794	-14.945	-6.769	-5.388	-4.725	-1.070	0.065	0.051	0.075
	σ^2	0.033	0.062	0.086	0.030	0.067	0.072	-14.177	-9.506	5.282
	p	**0.002**	**<0.001**	**0.001**	**0.003**	**0.009**	0.182	**<0.001**	**<0.001**	**0.003**
N_{branch}/V	t-value	-7.313	-13.901	-12.492	-3.425	-8.079	-1.541	-11.029	-6.941	5.171
	σ^2	0.383	0.576	0.245	0.406	0.151	0.386	0.554	0.478	0.435
	p	**0.003**	**<0.001**	**0.001**	**0.021**	**0.001**	0.110	**<0.001**	**0.001**	**0.003**
τ avr	t-value	-4.483	-2.735	-5.810	1.617	2.585	0.780	4.730	4.946	0.048
	σ^2	0.022	0.010	0.003	0.016	0.010	0.006	0.016	0.015	0.007

	p	**0.005**	**0.026**	**0.014**	0.091	0.061	0.258	**0.009**	**0.008**	0.482
τ direction x	t-value	-4.518	-2.328	-6.411	2.908	5.183	1.045	4.565	4.762	-0.052
	σ^2	0.031	0.008	0.002	0.007	0.003	0.004	0.033	0.030	0.006
	p	**0.023**	**0.040**	**0.004**	**0.022**	**0.018**	0.203	**0.010**	**0.021**	0.481
τ direction y	t-value	-2.726	-3.703	-2.660	1.736	2.557	0.385	0.329	1.718	1.613
	σ^2	0.022	0.017	0.011	0.006	0.004	0.007	0.032	0.028	0.020
	p	**0.050**	**0.017**	**0.038**	0.090	**0.031**	0.360	0.379	0.092	0.091
τ direction z	t-value	-4.548	-0.813	-3.899	1.587	3.261	0.656	5.000	3.833	-1.416
	σ^2	0.030	0.026	0.012	0.024	0.010	0.015	0.033	0.032	0.023
	p	**0.010**	0.231	**0.030**	0.094	**0.041**	0.290	**0.004**	**0.009**	0.115
Pore size distribution										
$VP_{0.001-0.01}$ (%)	t-value	-14.449	-7.777	-6.000	6.658	4.275	-1.587	11.567	15.076	0.739
	σ^2	0.222	0.200	0.175	0.156	0.221	0.152	0.265	0.175	0.222
	p	**<0.001**	**0.002**	**0.002**	**0.003**	**0.006**	0.105	**<0.001**	**<0.001**	0.257
$VP_{0.01-0.1}$ (%)	t-value	-11.488	-6.808	-4.337	5.246	4.066	-0.465	14.042	15.396	1.534
	σ^2	0.409	0.218	0.320	0.356	0.478	0.468	0.271	0.251	0.069
	p	**<0.001**	**0.003**	**0.025**	**0.003**	**0.008**	0.333	**<0.001**	**0.002**	0.100
$VP_{0.1-1}$ (%)	t-value	-14.466	-4.196	1.289	10.111	10.430	-0.020	10.421	18.023	0.726
	σ^2	0.211	0.344	0.039	0.086	0.080	0.019	0.469	0.177	0.372
	p	**<0.001**	**0.026**	0.144	**0.001**	**0.005**	0.493	**0.001**	**<0.001**	0.272
VP_{1-10} (%)	t-value	-11.207	-5.360	-4.915	27.822	27.637	0.126	13.757	13.469	-0.887
	σ^2	1.081	0.017	0.033	0.015	0.015	0.001	1.083	1.099	0.049
	p	**0.004**	**0.017**	**0.019**	**0.001**	**0.001**	0.453	**0.003**	**0.003**	0.213
$VP_{>10}$ (%)	t-value	8.542	3.357	4.333	-3.989	-3.550	0.619	-9.350	-12.737	-0.323
	σ^2	14.425	8.536	3.301	9.176	9.863	2.283	13.785	7.863	9.555
	p	**0.001**	**0.039**	**0.006**	**0.029**	**0.019**	0.285	**<0.001**	**0.001**	0.384
Pore shape distribution										
VP_{Eq} (%)	t-value	-4.005	-1.293	0.889	-3.191	-2.991	0.322	-0.326	2.194	2.790
	σ^2	0.741	0.818	0.508	0.658	0.594	0.768	0.901	0.655	0.558
	p	**0.008**	0.133	0.220	**0.017**	**0.020**	0.382	0.380	**0.050**	**0.034**
VP_{Pr} (%)	t-value	-1.595	4.609	-1.490	-1.943	-1.566	0.007	2.407	-1.178	-5.476
	σ^2	2.333	0.309	1.333	1.323	2.022	1.032	1.319	1.643	0.609
	p	0.093	**0.005**	0.105	0.074	0.096	0.497	0.069	0.162	**0.006**

VP_{Ob} (%)	t-value	2.360	0.608	-0.030	1.395	1.643	0.099	-0.235	-0.752	-0.747
	σ^2	1.645	1.379	1.388	2.292	1.886	2.113	0.733	1.147	0.654
	p	**0.039**	0.303	0.489	0.118	0.088	0.463	0.415	0.247	0.255
VP_{Tr} (%)	t-value	2.344	-1.614	0.674	2.524	2.138	-0.369	-1.580	0.306	1.591
	σ^2	1.486	1.703	2.764	1.153	1.134	1.384	2.035	3.116	3.083
	p	**0.050**	0.091	0.274	**0.033**	**0.050**	0.366	0.095	0.387	0.093

P = Porosity by image; NP = Number of Pores; DA = Degree of anisotropy; EPC/V = Connectivity (EPC/V); N_{junc} = Number of junctions; N_{branch} = Number of branches; $\tau_{average}$ = Average tortuosity; τ_x. τ_y and τ_z = tortuosity in the directions x, y and z, respectively; $VP_{0.0001\text{-}0.01\ mm^3}$, $VP_{0.01\text{-}0.1\ mm^3}$, $VP_{0.1\text{-}1\ mm^3}$, $VP_{1\text{-}10\ mm^3}$ and $VP_{>10\ mm^3}$ = Volume of pores between 0.0001 to 0.01 mm^3, 0.01 to 0.1 mm^3, 0.1 to 1 mm^3, 1 to 10 mm^3 and >10 mm^3, respectively; VP_{Eq}, VP_{Pr}, VP_{Ob} and VP_{Tr} = Volume of equant, prolate, oblate and triaxial shaped pores. **p*≤0.05. n=3 (number of samples analyzed for each treatment).